Supplementary Information

Trace Pd Modified Intermetallic PtBi Nanoplates towards Efficient Formic Acid Electrocatalysis

Min Tang, Wen Chen, Shuiping Luo, Xiaotong Wu, Xiaokun Fan, Yujia Liao, Xing Song, Yu Cheng, Lanxi Li, Li Tan, Yulian Liu, Zewei Quan*

Department of Chemistry, Guangdong Provincial Key Laboratory of Energy Materials for Electric Power, Southern University of Science and Technology (SUSTech), Shenzhen, Guangdong, 518055, China.

* Correspondence author: E-mail: quanzw@sustech.edu.cn

Experimental

Chemicals:

The chemical reagents used in the experiment were as follows: Platinum (II) acetylacetonate [$Pt(acac)_2$, 98%] were purchased from Energy Chemical. Palladium acetylacetone [$Pd(acac)_2$, 99%] were purchased from Shanghai Aladdin Biochemical Technology. Bismuth acetate [$Bi(act)_3$, 99.99%] was purchased from Shanghai Macklin Biochemical Technology. Oleylamine (OAm, 70%), octadecene (ODE, 90%), cetyltrimethyl ammonium bromide (CTAB, ≥99.0%) were purchased from Sigma-Aldrich. Ascorbic acid (AA, 99%) was purchased from Shanghai Aladdin Biochemical Technology. The commercial Pt/C catalyst (20 wt.% Pt on Vulcan XC-72 carbon, Pt particle size 2 to 5 nm) was obtained from Johnson Matthey Corporation. The commercial Pd black (98 wt.% Pd, surface area 28-32 $m^2 g^{-1}$) was obtained from Acros Organics. All the chemicals were used as received without further purification. The water used in all experiments was ultrapure water (18.2 MΩ cm^{-1}).

Preparation of intermetallic PtBi hexagonal nanoplates:

In a typical synthesis of intermetallic PtBi hexagonal nanoplates, 5 mL of OAm and 5 mL of ODE were added into the vial with a capacity of 40 mL. Then, 20.4 mg of $Pt(acac)_2$, 20.0 mg of $Bi(act)_3$, 80 mg of AA and 350 mg of CTAB were added into the solution, and the vial was sealed. At the first step, the vial was placed in a heating module at 80 °C for 1 h. At the same time, another heating module was heated to 220 °C. At the second step, the vial was transferred to the above heating module and maintained at 220°C for 1 h. Finally, the vial was naturally cooled to room temperature. The obtained product was washed three times by ethanol/n-hexane mixture with a volume ratio of 2:1, and after thoroughly mixing in an ultrasonic machine, the product was obtained by centrifugation of 5000 rpm. Finally, in order to wash away the organic

ligands such as OAm or CTAB contained in the surface of the nanoplate, it was washed five times with a mixture of ethanol and n-hexane.

Preparation of PtBi@Pd hexagonal nanoplates with different Pd compositions:

In a typical synthesis of PtBi@Pd hexagonal nanoplates, 5 mL of OAm and 5 mL of ODE were added into the vial with a capacity of 40 mL. Then, 20.4 mg of $Pt(acac)_2$, 20.0 mg of $Bi(act)_3$, 80 mg of AA and 350 mg of CTAB were added into the solution, and the vial was sealed. At the first step, the vial was placed in a heating module at 80 °C for 1 h. At the same time, another heating module was heated to 220 °C. At the second step, the vial was transferred to the above heating module and maintained at 220°C for 1 h. Then, the vial was transferred to a heating module and maintained at 140°C for 10 min. By now, 51.0 mg of $Pd(acac)_2$ was dissolved in 5 mL of OAm and 5 mL of ODE, and the $Pd(acac)_2$ concentration of this obtained solution is 5.1 mg mL^{-1}. Finally, different amount of $Pd(acac)_2$ solution was added very slowly into the above vial, and was maintained at 190°C for 1 h. Then, the vial was naturally cooled to room temperature. The obtained product was washed three times by ethanol/n-hexane mixture with a volume ratio of 2:1, and after thoroughly mixing in an ultrasonic machine, the product was obtained by centrifugation of 5000 rpm. Finally, in order to wash away the organic ligands such as OAm or CTAB contained in the surface of the nanoplate, it was washed five times with a mixture of ethanol and n-hexane.

Characterization:

The transmission electron microscopy (TEM) characterization of the obtained material was performed using a Hitachi HT7700 (100 kV). Some high-angle annular dark-field scanning transmission electron microscopy (HAADF-STEM) images and energy dispersive spectroscopy (EDS) results was performed using FEI Talos F200X TEM (200 kV). High resolution HAADF-STEM images and EDS mapping images were obtained on a FEI Titan Cubed Themis G2 equipped with double corrected spherical aberration (300 kV). X-ray diffraction (XRD) patterns were recorded using an Rigaku SmartLab X-ray diffractometer with Cu Kα radiation (λ= 0.15418 nm). X-ray photoelectron spectroscopy (XPS) was performed on a PHI 5000 Versaprobe III XPS spectrometer with Al Kα as the excitation source. Elementary composition was determined by inductively coupled plasma mass spectrometry (ICP-MS) manufactured by Agilent 7700x.

Electrochemical measurements:

The electrochemical measurements were performed by using a three-electrode cell with a PINE Instrument Bipotentiostat. Glassy-carbon disk electrodes (RDE) (diameter: 5 mm, area: 0.2475 cm^2) from Pine Instruments was used as working electrode. The reference electrode was saturated calomel electrode (SCE). The counter electrode was a carbon rod. The Pt loadings of catalysts on the glassy-carbon electrode were based on ICP-MS analysis. About 10 μL of catalyst ink containing 3.2 μg of Pt+Pd were dropwise added on the working electrode by using a micro syringe, and then the electrode was dried at room temperature.

The cyclic voltammetry (CV) was carried out at room temperature in Ar-saturated 0.5 M H_2SO_4 solution between -0.2–1.0 V (vs. SCE) at a scan rate of 50 mV s^{-1}. For the electro-oxidation of formic acid, the CV curves were recorded in 0.5 M H_2SO_4 + 1.0 M HCOOH between -0.2–0.8 V (vs. SCE) at a scan rate of 50 mV s^{-1}. The accelerated durability tests were performed between -0.2–0.6 V (vs. SCE) at a scan rate of 50 mV s^{-1} for 1000 cycles. The chronoamperometry was conducted at 0.2 V vs. SCE in 0.5 M H_2SO_4 + 1.0 M HCOOH. For CO-stripping tests, CO was used to saturate the 0.5 M H_2SO_4 electrolyte for 30 min, while holding the working electrode at -0.14 V (vs. SCE), and then the remaining CO was thoroughly purged with high-purity Ar gas for 30 min. Afterwards, the CV curves of CO-stripping were obtained a in Ar-saturated 0.5 M H_2SO_4 solution between -0.2–1.0 V (vs. SCE) at a scan rate of 50 mV s^{-1}.

Table S1. The catalytic activities of some recently reported representative Pt-based and Pd-based electrocatalysts towards FAOR under acidic conditions. All the mass activities represent the forward peak current densities of different catalysts.

Catalysts	Electrolyte	Mass activity (A mg^{-1})	Peak potential (V)	Dominant Path	Reference
PtBi@1.8% Pd HNPs	0.5 M H_2SO_4 1 M HCOOH	4.17	0.41 (vs. SCE)	Direct	This work
Pt_4Au_{96} Single Pt Atom	0.1 M $HClO_4$ 0.1 M HCOOH	3.77	0.50 (vs. RHE)	Direct	1 Nature Materials, 2018
Mesoporous Palladium Nanotube Arrays	0.5 M H_2SO_4 0.5 M HCOOH	3.65	0.32 (vs. SCE)	Direct	2 Advanced Energy Materials, 2019.
$Pd_{59}Cu_{30}Co_{11}$ Dendrites	0.1 M $HClO_4$ 0.5 M HCOOH	5.32	0.67 (vs. Ag/AgCl)	Indirect	3 Nature Communications, 2018.
Intermetallic PtBi Nanoplatelets	0.5 M $HClO_4$ 0.5 M HCOOH	1.8	0.40 (vs. Ag/AgCl)	Direct	4 Nanoscale, 2014.
Defect-rich Cubic Intermetallic Pt_3Sn	0.1 M $HClO_4$ 1 M HCOOH	0.58	0.91 (vs. RHE)	Indirect	5 Advanced Materials, 2016.
Intermetallic $Pt_{45}Sn_{25}Bi_{30}$	0.5 M H_2SO_4 1 M HCOOH	4.39	0.41 (vs. SCE)	Direct	6 Advanced Materials, 2019.
Intermetallic $PtCo_{0.5}Ni_{0.5}$	0.5 M H_2SO_4 0.5 M HCOOH	2.15	1.02 (vs. RHE)	Indirect	7 Journal of Materials Chemistry, 2018.
Sea Urchin-like $Au_{71}@Pd_{29}$	0.5 M H_2SO_4 0.5 M HCOOH	1.41	0.23 (vs. SCE)	Direct	8 Applied Catalysis B: Environmental, 2020.
Pd–Cu Tripods	0.5 M $HClO_4$ 0.5 M HCOOH	1.58	0.54 (vs. RHE)	Direct	9 Advanced Functional Materials, 2014.

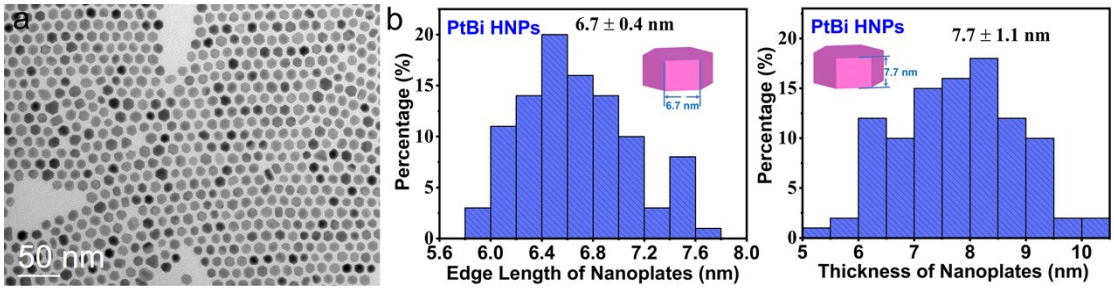

Figure S1. **(a)** Typical TEM image of PtBi HNPs. **(b)** Size distribution of the edge length, and thickness of PtBi HNPs.

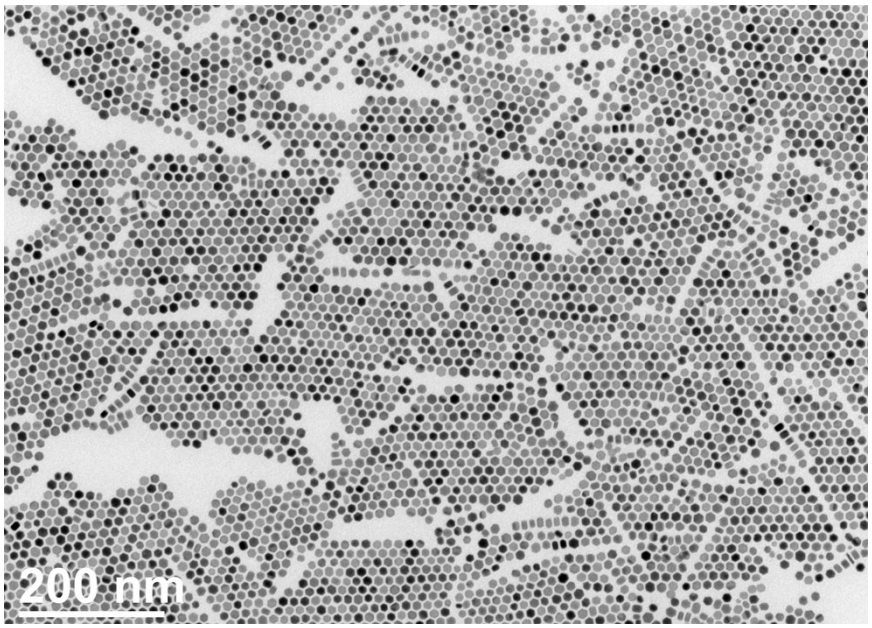

Figure S2. Typical low-magnification TEM image of PtBi@1.8% Pd HNPs.

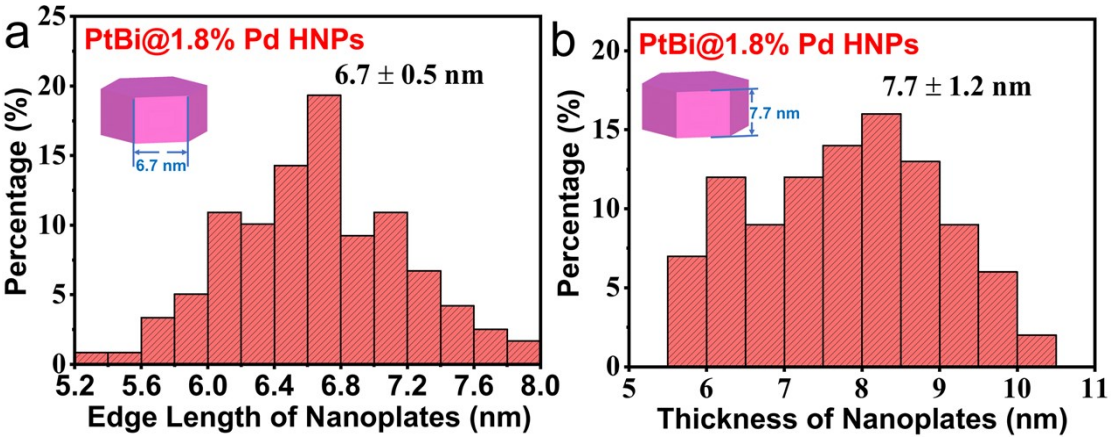

Figure S3. Size distribution of the **(a)** edge length and **(b)** thickness of PtBi@1.8% Pd HNPs.

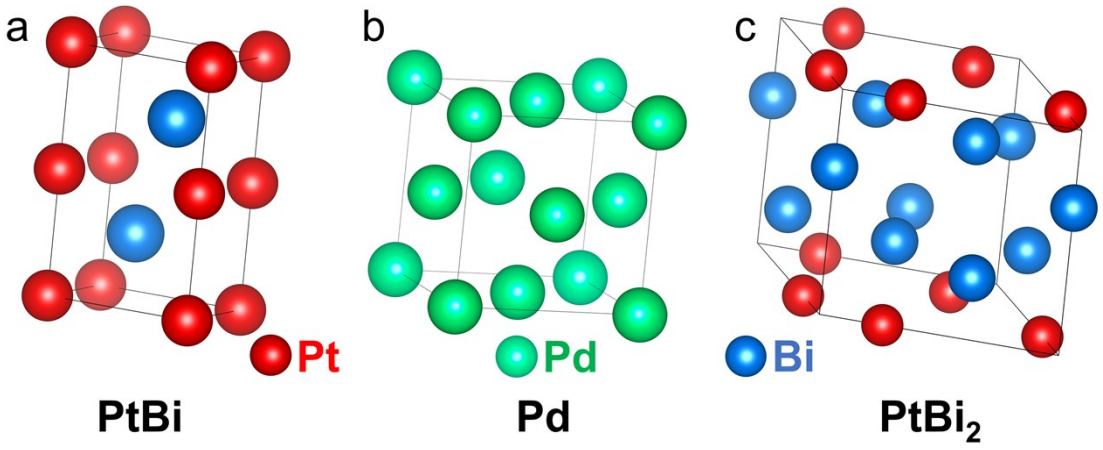

Figure S4. Unit cells of **(a)** PtBi [P63/mmc, JCPDS No. 61-6981], **(b)** Pd [Fm-3m, JCPDS No. 87-0637], and **(c)** $PtBi_2$ [P31m, JCPDS No. 42-8088].

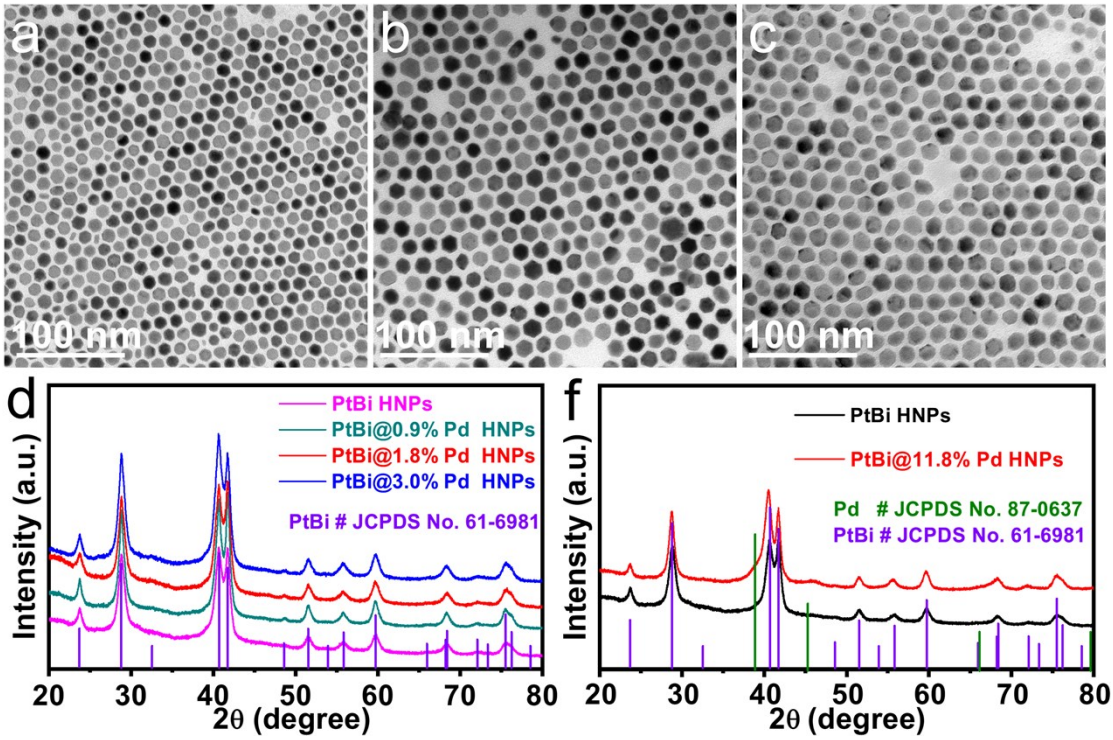

Figure S5. Typical TEM image of **(a)** PtBi@0.9% Pd HNPs, **(b)** PtBi@3.0% Pd HNPs, and **(c)** PtBi@11.8% Pd HNPs. **(d)** Powder XRD patterns of PtBi HNPs and PtBi@Pd HNPs with different Pd compositions. **(e)** Powder XRD patterns of PtBi@11.8% Pd HNPs. The standard diffraction peaks of hcp PtBi (JCPDS No. 61-6981) and fcc Pd (JCPDS No. 87-0637) are demonstrated as comparisons in the figure.

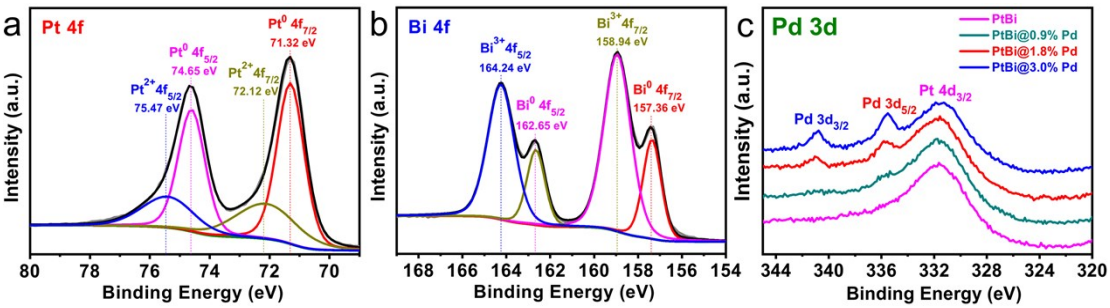

Figure S6. XPS spectra of **(a)** Pt 4f and **(b)** Bi 4f of PtBi@1.8% Pd HNPs. **(c)** XPS spectra of Pd 3d of PtBi@Pd HNPs with different Pd compositions.

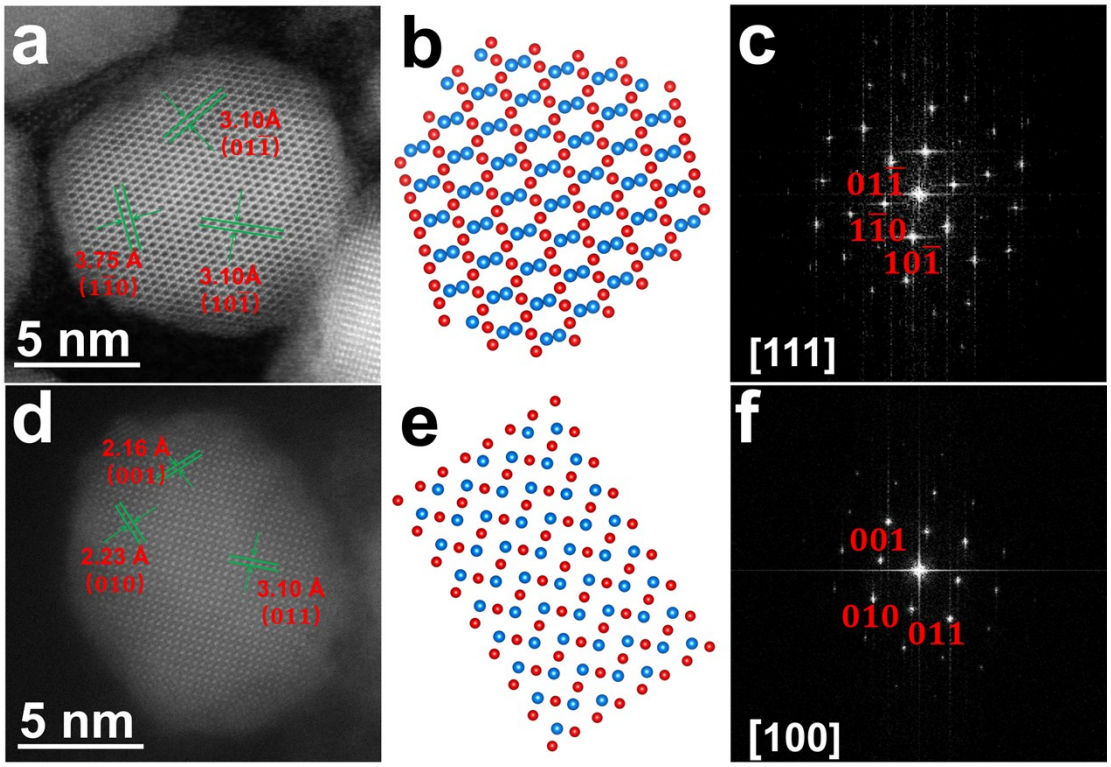

Figure S7. **(a)** Atomic resolution HAADF-STEM image, **(b)** Crystal model, and **(c)** FFT pattern of PtBi HNPs along the [111] zone axis. **(d)** Atomic resolution HAADF-STEM image, **(e)** Crystal model, and **(f)** FFT pattern of PtBi HNPs along the [100] zone axis.

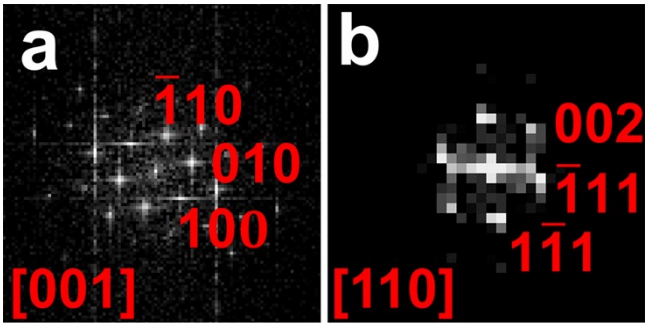

Figure S8. **(a)** Corresponding fast Fourier transformation (FFT) pattern of PtBi@1.8% Pd HNPs in the red rectangle viewed along hcp PtBi [001] zone axis. **(b)** Corresponding fast FFT pattern of PtBi@1.8% Pd HNPs in the green rectangle viewed along fcc Pd [110] zone axis.

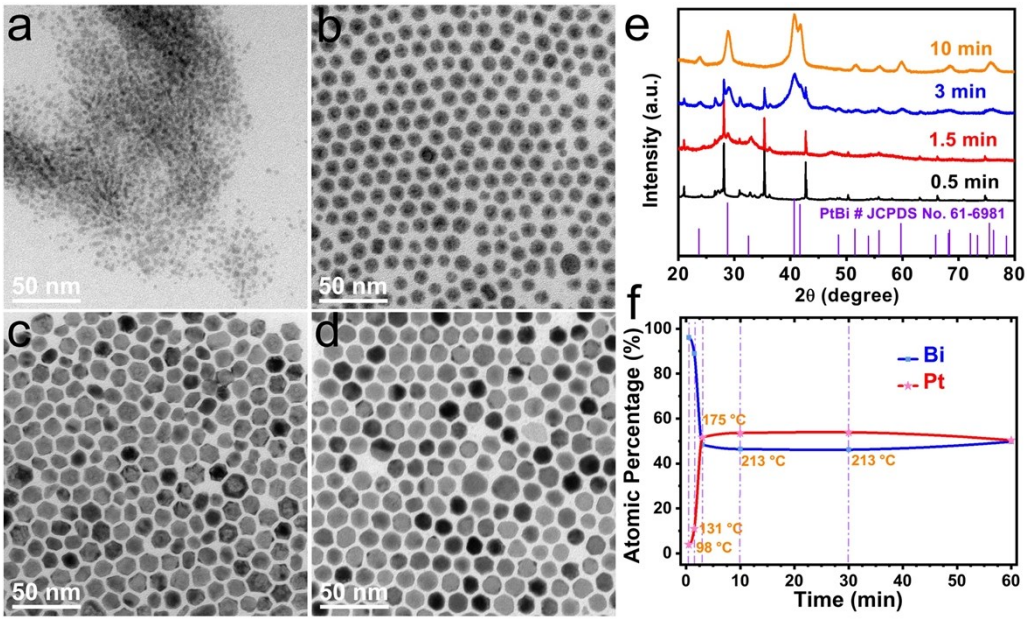

Figure S9. Typical TEM images of produced intermediates of PtBi HNPs obtained at different reaction time of **(a)** 0.5 min, **(b)** 1.5 min, **(c)** 3 min, and **(d)** 10 min.

After an initial growth period of 0.5 min, when the reaction temperature rose from 80 to 98 ℃, the bismuth was mainly reduced with a Pt/Bi atomic ratio of 3.9/96.1, then small-sized nanoparticles of different shapes were obtained, which served as the nuclei for further growth (**Figures S9a** and **S9f**). Sharp diffraction peaks will appear in the XRD pattern, which were considered as the peak of bismuth complex (**Figure S9e**). When the reaction time was increased to 1.5 min (131 ℃), hetero-structured nanoparticles with a diameter of 11.0 ± 0.4 nm were obtained (**Figures S9b** and **S9e**). Determined by EDS elemental mapping images and line-scan profile (**Figure S10**), Bi is evenly distributed on the nanoparticles, while Pt is mainly distributed in the central part, where the image was brighter than outer part. In consequence, Pt gradually replace some bismuth atoms at this stage. However, it is not enough to change its phase on account of the low composition of Pt (Pt/Bi = 11.1/88.9). When the reaction time was extended to 3 min (175 ℃), the nanoparticles gradually grew into irregular hexagonal nanoplates with a larger size (side length of 6.6 ± 0.6 nm, **Figure S9c**), of which atomic ratio of Pt/Bi was 51.6/48.4 (**Figure S9f**). At this stage, diffraction peaks of PtBi and bismuth complex appear together in the XRD pattern (**Figure S9e**). Furthermore, when the reaction time was increased to 10 min (213 ℃), the irregular hexagonal nanoplates changed into more regular hexagonal nanoplates (**Figure S9d**), and the diffraction peaks of bismuth complex fade away (**Figure S9e**).

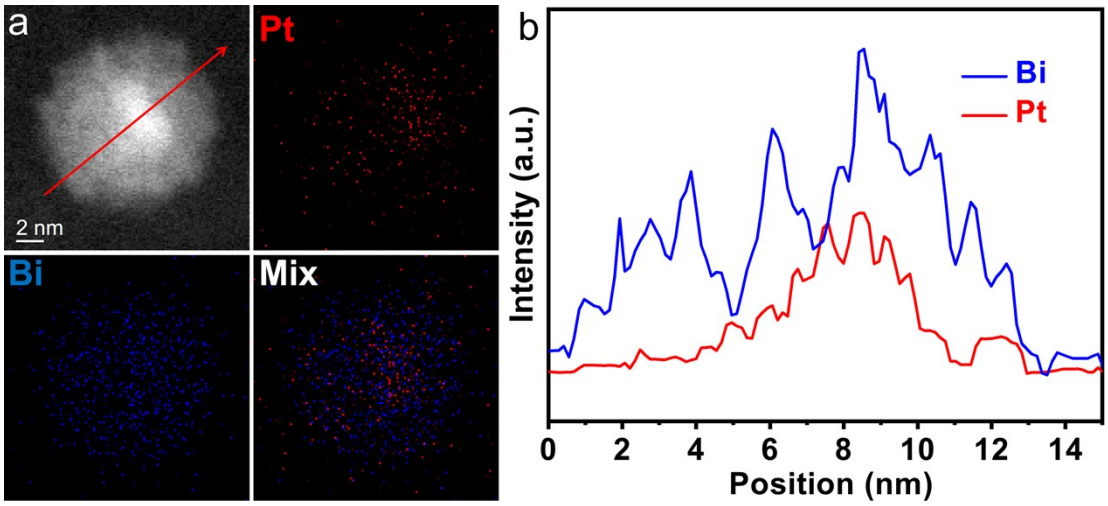

Figure S10. **(a)** EDS elemental mapping images and **(b)** EDS elemental line-scan profiles of produced intermediates of PtBi nanoparticles obtained at reaction time of 1.5 min.

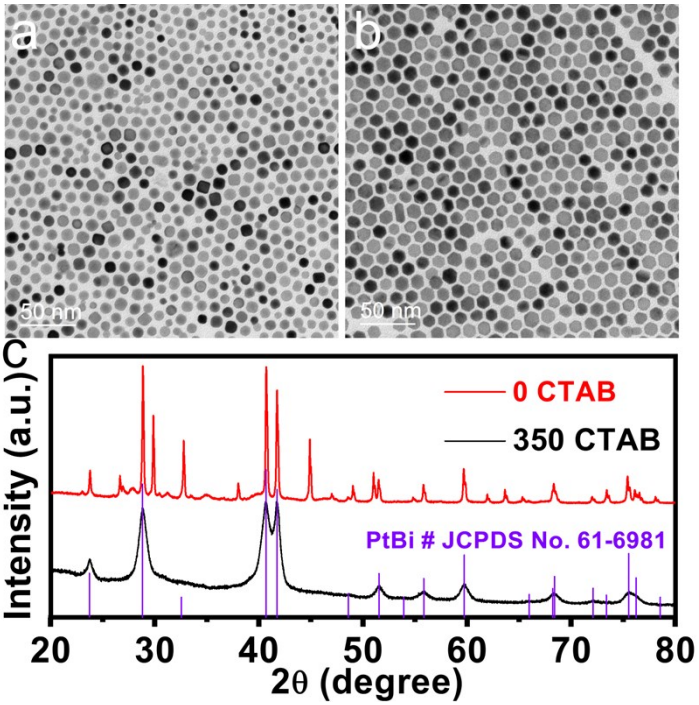

Figure S11. Typical TEM images of as-prepared nanocrystals when the amount of added CTAB was **(a)** 0 mg, and **(b)** 350 mg. **(c)** Corresponding XRD patterns of the above two samples.

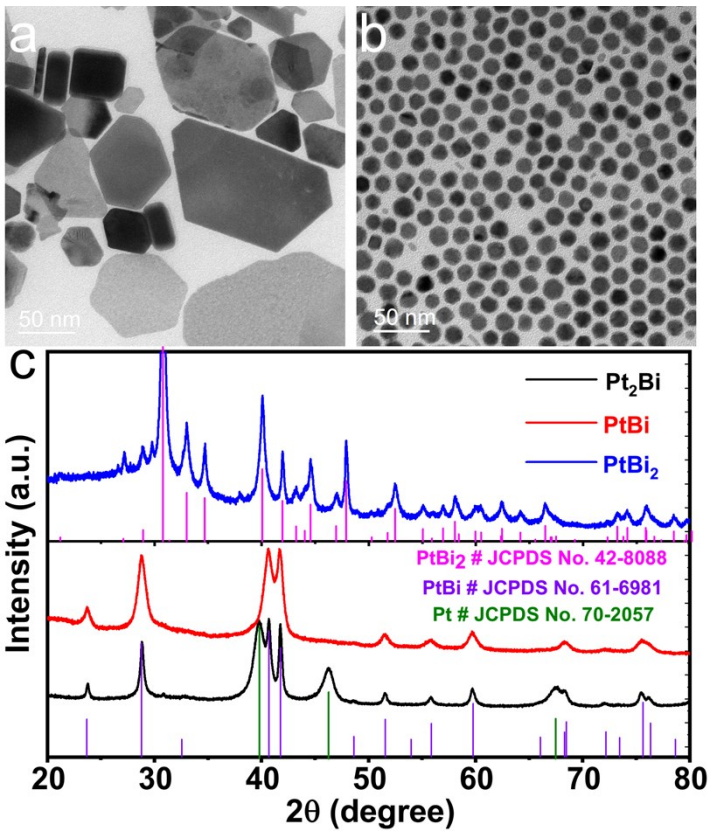

Figure S12. Typical TEM images of as-prepared nanocrystals when the atomic feed ratio of Pt/Bi precursors was **(a)** 2:1, and **(b)** 1:2. **(c)** Corresponding XRD patterns of the above two samples.

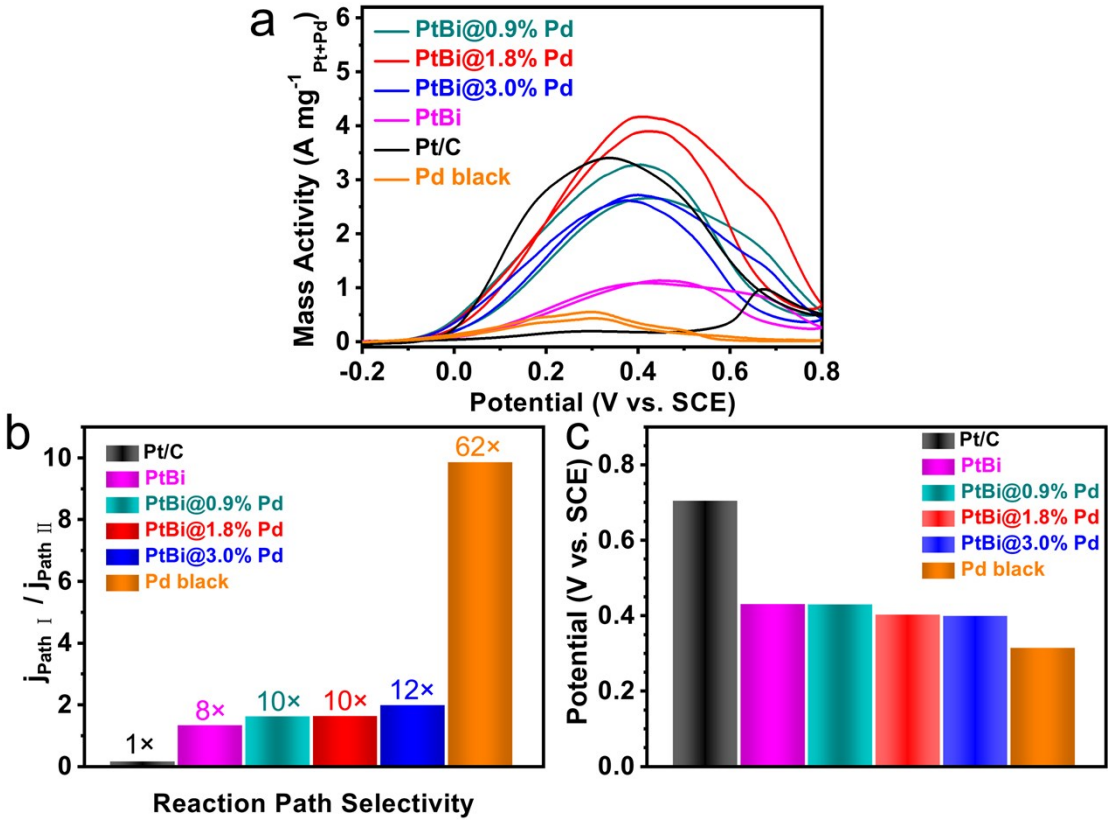

Figure S13. **(a)** Anode polarization curves of cyclic voltammograms towards FAOR of different catalysts in Ar-saturated 0.5 M H_2SO_4 + 1.0 M HCOOH solution at a scan rate of 50 mV s^{-1}. **(b)** Histogram on ratios of the peak current densities ($j_{path\ I}/j_{path\ II}$) of different catalysts on the peak (≈ 0.40 V, direct path Ⅰ) and peak (≈ 0.68 V, indirect path Ⅱ). **(c)** Histogram of peak potentials on the anode polarization curves of different catalysts.

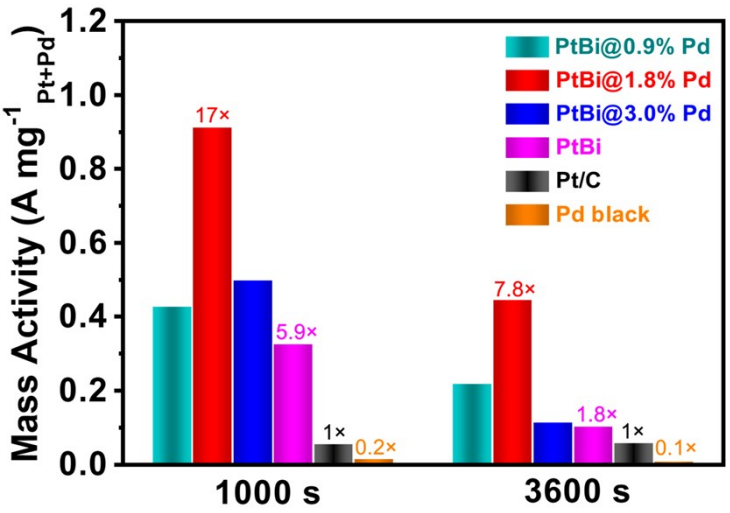

Figure S14. Histogram of mass activities of different catalysts after 1000 s and 3600 s recorded at 0.2 V (vs. SCE) in Ar-saturated 0.5 M H_2SO_4 + 1.0 M HCOOH solution.

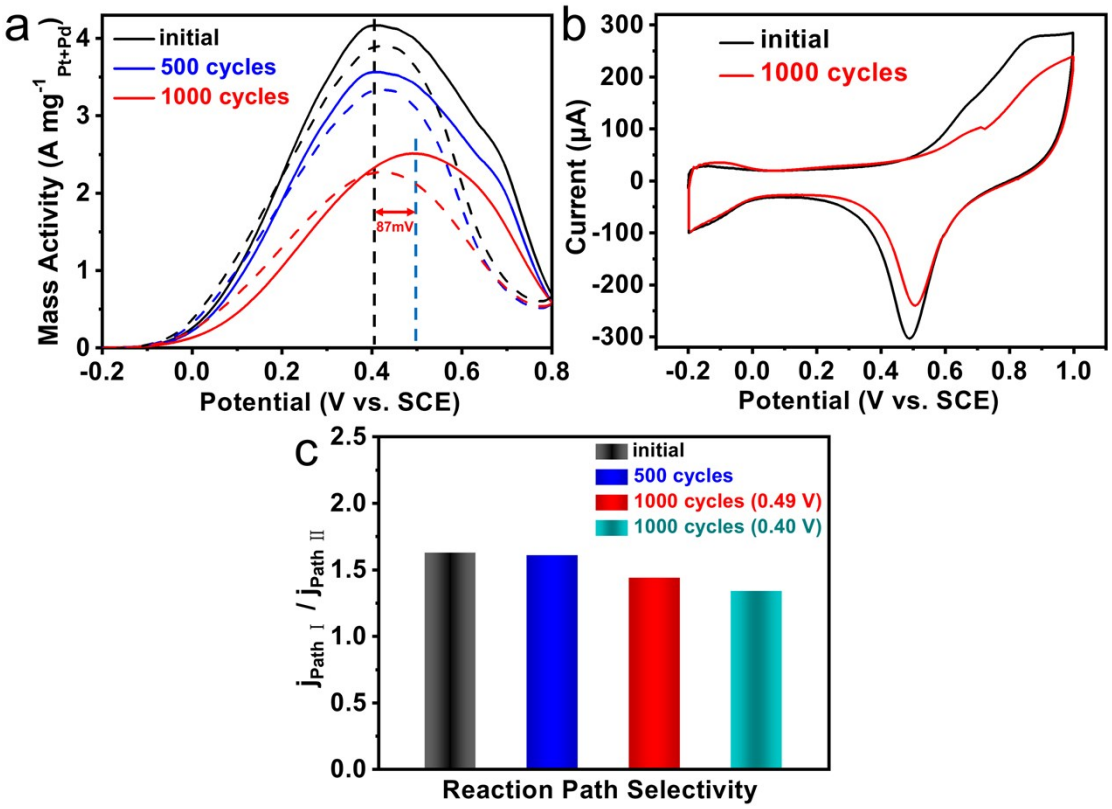

Figure S15. **(a)** Anode polarization curves towards FAOR of PtBi@1.8% Pd HNPs after different potential cycles between -0.2 and 0.6 V (vs. SCE) in Ar-saturated 0.5 M H_2SO_4 + 1.0 M HCOOH solution at a scan rate of 50 mV s^{-1}. The solid line represents the forward sweep curve, while the dotted line represents the backward sweep curve. **(b)** Cyclic voltammetric curves of the PtBi@1.8% Pd HNPs before and after 1000 cycles in Ar-saturated 0.5 M H_2SO_4 solution at a scan rate of 50 mV s^{-1}. (c) Histogram on ratios of the peak current densities ($j_{path\ Ⅰ}/j_{path\ Ⅱ}$) of PtBi@1.8% Pd HNPs after different potential cycles on the peak (≈ 0.40 V or 0.49 V, direct path Ⅰ) and peak (≈ 0.68 V, indirect path Ⅱ).

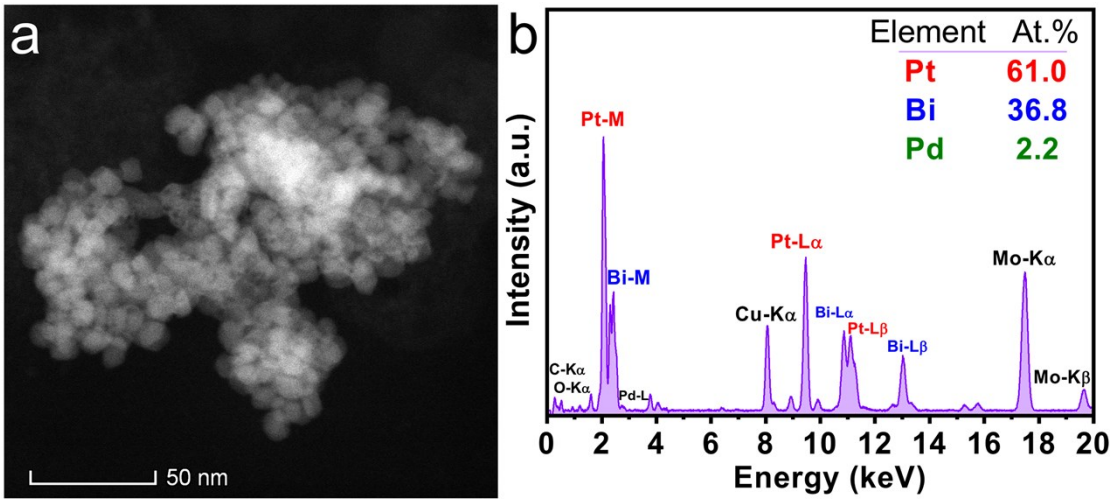

c

Sample	Pt	Bi	Pd
PtBi	71.7%	28.3%	0.0%
PtBi@1.8% Pd	61.0%	36.8%	2.2%
PtBi@3.0% Pd	56.7%	39.7%	3.6%

Figure S16. **(a)** HAADF-STEM image and **(b)** TEM-EDS spectrum of PtBi@1.8% Pd HNPs after 1000 potential cycles in Ar-saturated 0.5 M H_2SO_4 + 1.0 M HCOOH solution at a scan rate of 50 mV s^{-1}. **(c)** Elemental compositions of PtBi, PtBi@1.8% Pd, and PtBi@3.0% Pd HNPs after 1000 cycles.

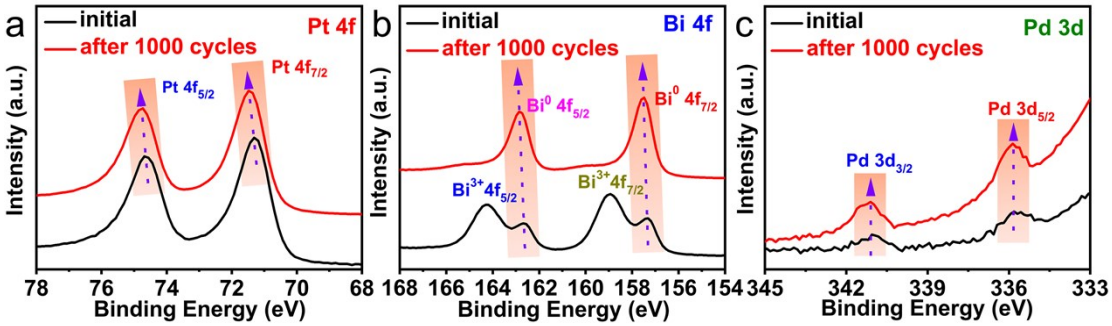

Figure S17. XPS spectra of the (a) Pt 4f, (b) Bi 4f and (c) Pd 3d of PtBi@1.8% Pd HNPs before and after 1000 potential cycles.

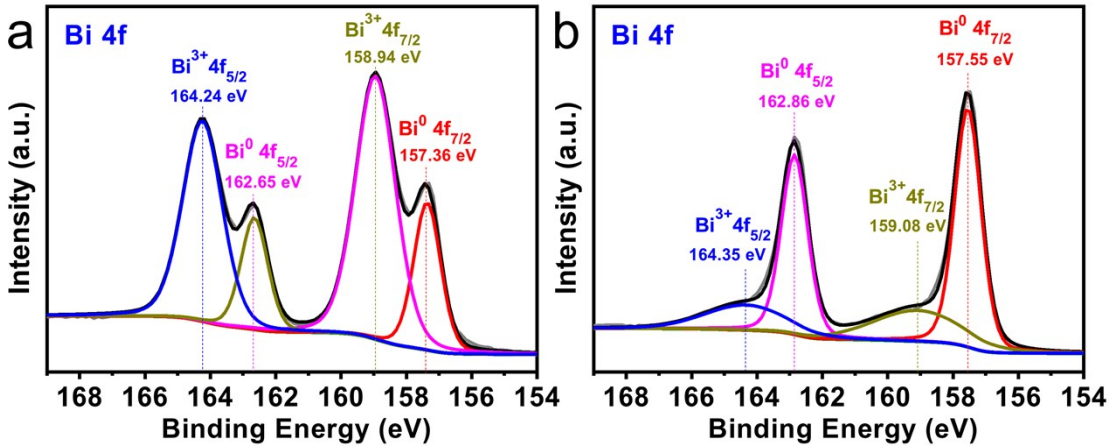

Figure S18. XPS spectra of the Bi 4f of PtBi@1.8% Pd HNPs (a) before, and (b) after 1000 potential cycles.

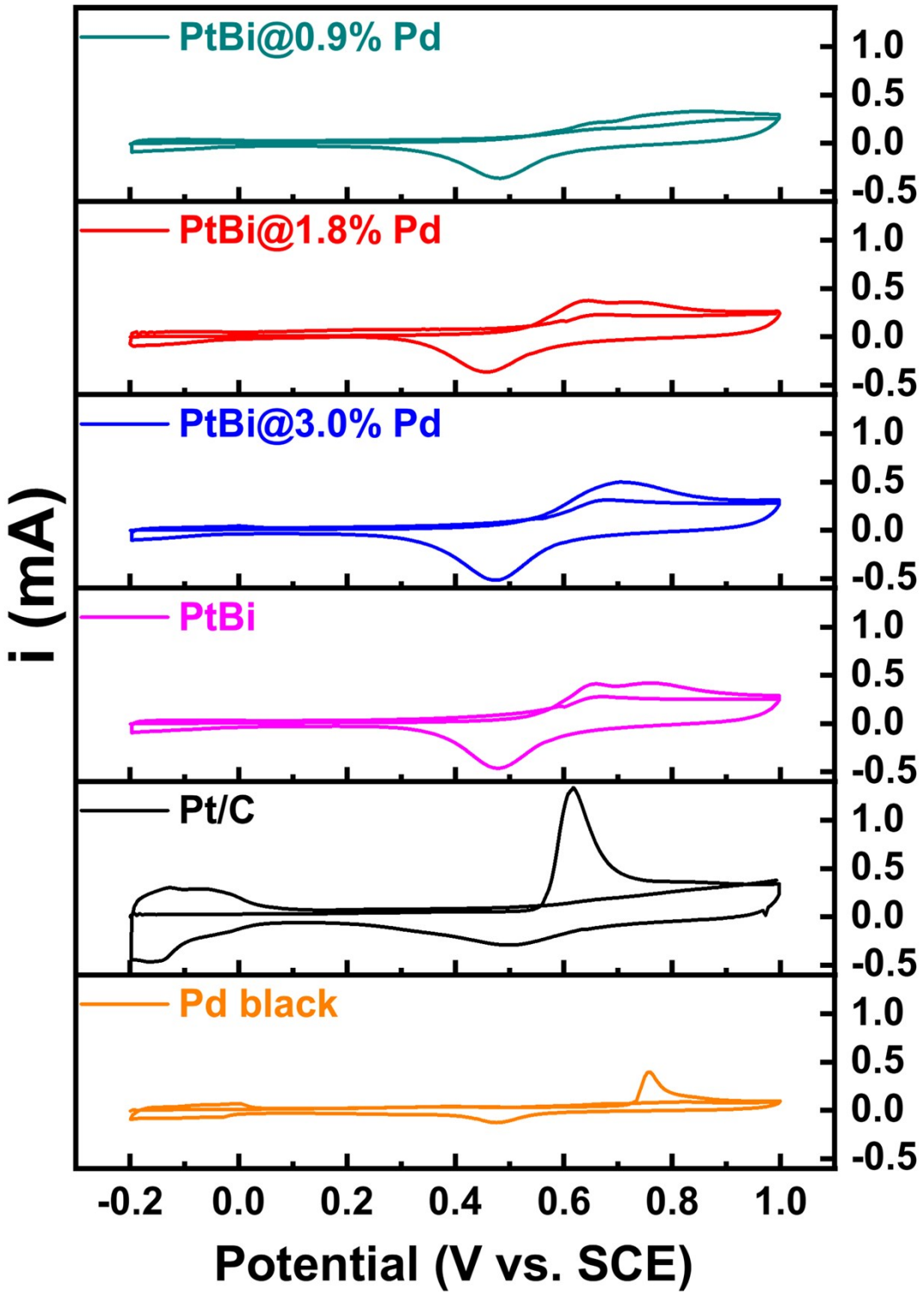

Figure S19. CO-stripping curves of different catalysts in 0.5 M H_2SO_4 solution at a scan rate of 50 mV s^{-1}.

References:

1. Duchesne, P. N.; Li, Z.; Deming, C. P.; Fung, V.; Zhao, X.; Yuan, J.; Regier, T.; Aldalbahi, A.; Almarhoon, Z.; Chen, S., Golden single-atomic-site platinum electrocatalysts. *Nature materials* **2018,** *17* (11), 1033-1039.

2. Ding, J.; Liu, Z.; Liu, X.; Liu, J.; Deng, Y.; Han, X.; Zhong, C.; Hu, W., Mesoporous Decoration of Freestanding Palladium Nanotube Arrays Boosts the Electrocatalysis Capabilities toward Formic Acid and Formate Oxidation. *Advanced Energy Materials* **2019,** *9* (25), 1900955.

3. Li, C.; Yuan, Q.; Ni, B.; He, T.; Zhang, S.; Long, Y.; Gu, L.; Wang, X., Dendritic defect-rich palladium–copper–cobalt nanoalloys as robust multifunctional non-platinum electrocatalysts for fuel cells. *Nature communications* **2018,** *9* (1), 1-9.

4. Liao, H.; Zhu, J.; Hou, Y., Synthesis and electrocatalytic properties of PtBi nanoplatelets and PdBi nanowires. *Nanoscale* **2014,** *6* (2), 1049-1055.

5. Rong, H.; Mao, J.; Xin, P.; He, D.; Chen, Y.; Wang, D.; Niu, Z.; Wu, Y.; Li, Y., Kinetically Controlling Surface Structure to Construct Defect-Rich Intermetallic Nanocrystals: Effective and Stable Catalysts. *Advanced Materials* **2016,** *28* (13), 2540-2546.

6. Luo, S.; Chen, W.; Cheng, Y.; Song, X.; Wu, Q.; Li, L.; Wu, X.; Wu, T.; Li, M.; Yang, Q., Trimetallic Synergy in Intermetallic PtSnBi Nanoplates Boosts Formic Acid Oxidation. *Advanced Materials* **2019,** *31* (40), 1903683.

7. Chen, L.; Zhu, J.; Xuan, C.; Xiao, W.; Xia, K.; Xia, W.; Lai, C.; Xin, H. L.; Wang, D., Effects of crystal phase and composition on structurally ordered Pt–Co–Ni/C ternary intermetallic electrocatalysts for the formic acid oxidation reaction. *Journal of Materials Chemistry A* **2018,** *6* (14), 5848-5855.

8. Yang, L.; Li, G.; Chang, J.; Ge, J.; Liu, C.; Vladimir, F.; Wang, G.; Jin, Z.; Xing, W., Sea urchin-like Aucore@Pdshell electrocatalysts with high FAOR performance: Coefficient of lattice strain and electrochemical surface area. *Applied Catalysis B: Environmental* **2020,** *260*, 118200.

9. Zhang, L.; Choi, S. I.; Tao, J.; Peng, H. C.; Xie, S.; Zhu, Y.; Xie, Z.; Xia, Y., Pd–Cu bimetallic tripods: a mechanistic understanding of the synthesis and their enhanced electrocatalytic activity for formic acid oxidation. *Advanced Functional Materials* **2014,** *24* (47), 7520-7529.